

Current Status of Inert Higgs Dark Matter with Dark Fermions

Yi-Zhong Fan^{1,2}, Yao-Yu Li^{1,2}, Chih-Ting Lu³, Xiao-Yi Luo³,

Tian-Peng Tang¹, Van Que Tran^{4,5}, Yue-Lin Sming Tsai^{1,2}

¹*Key Laboratory of DM and Space Astronomy, Purple Mountain Observatory,
Chinese Academy of Sciences, Nanjing 210033, China*

²*School of Astronomy and Space Science,
University of Science and Technology of China, Hefei, Anhui 230026, China*

³*Department of Physics and Institute of Theoretical Physics,
Nanjing Normal University, Nanjing, 210023, China*

⁴*Tsung-Dao Lee Institute & School of Physics and Astronomy,
Shanghai Jiao Tong University, Shanghai 200240, China and*

⁵*Phenikaa Institute for Advanced Study, Phenikaa University,
Yen Nghia, Ha Dong, Hanoi 100000, Vietnam*

Abstract

The precision measurements of the muon magnetic moment and the W boson mass have sparked interest in the potential deviations from standard model (SM) predictions. While it may be premature to attribute any excesses in these precision measurements to new physics, they do offer a valuable indication of potential directions for physics beyond the SM. Additionally, the particle nature of dark matter (DM) remains a crucial enigma. Despite the absence of any definitive DM signal in direct detection and collider experiments, the Galactic Center GeV γ -ray excess and the AMS-02 antiproton (\bar{p}) excess could potentially offer hints related to the evidence of DM. Motivated by these observations, we propose a simple DM model that addresses all these issues. This model extends the SM by incorporating singlet and doublet Dirac fermion fields, along with a doublet complex scalar field. For the viable parameter regions in this model, we find that future upgrades of the Large Hadron Collider and DM direct detection experiments can only partially probe them, while future high-energy muon colliders hold promise for exploring the unexplored parameter space.

I. INTRODUCTION

Although the particle standard model (SM) has achieved remarkable success with countless experimental confirmations, two clouds still loom over it due to recent precision measurements of the muon magnetic moment and the W boson mass. The former measurement was updated from the Fermilab experiment [1], and the new world average was reported as $a_\mu^{\text{Exp}} = 116592059(22) \times 10^{-11}$, which deviates from the SM prediction by 5.1σ (1.8σ) when the hadronic vacuum polarization (HVP) is calculated using the data-driven method [2] (lattice calculation method [3]). The root cause of this tension in the HVP contribution from these two methods remains unsolved, prompting the question of whether new physics effects are involved in this discrepancy. The latter measurement was reported by the CDF collaboration at Fermilab with $m_{W,\text{CDF II}} = 80.4335 \pm 0.0094$ GeV [4], revealing about a 7σ deviation from the SM prediction ($m_{W,\text{SM}} = 80.360 \pm 0.006$ GeV). In contrast, the ATLAS collaboration reported their W boson mass measurement $m_{W,\text{ATLAS}} = 80.360 \pm 0.016$ GeV [5], and very recently the CMS collaboration reported $m_{W,\text{CMS}} = 80.3602 \pm 0.0099$ GeV [6], which is consistent with the SM prediction but as precise as the CDF II measurement. This discrepancy raises another puzzle, and further data are needed to confirm whether new physics effects are at play. Therefore, these excesses from the two precision measurements may unveil new physics beyond the SM, even without finding any evidence of new particles.

On the other hand, the dark matter (DM) problem remains unsolved. Strong astrophysical and cosmological evidence supports the existence of DM [7]. Yet, apart from gravitational interaction, the particle nature of DM remains unknown. Among various DM candidates, Weakly Interacting Massive Particles (WIMPs) [8, 9] are well-motivated and popular. WIMPs have masses around the electroweak scale, and their interaction strength with SM particles is expected to be close to the weak interaction. Due to their predictability, there are ongoing DM direct detection [10], DM indirect detection [11], and collider experiments [12] dedicated to searching for WIMPs. Although DM direct detection [13, 14] and collider experiments [15] have placed strong constraints on WIMPs, there are still some potential pieces of evidence from DM indirect detection. For example, the galactic center GeV excess (GCE) [16–19] and the AMS-02 antiproton (\bar{p}) excess [20–23] provide indications that warrant further investigation.

	Fermion Fields				Scalar Fields	
	M_L	μ_R	Ψ	χ	H_1	H_2
$SU(2)_L$	2	1	2	1	2	2
$U(1)_Y$	-1/2	-1	-1/2	0	+1/2	+1/2
Z_2	+	+	-	-	+	-

TABLE I: Contents of fermion and scalar fields and their charge assignment under the $SU(2)_L \times U(1)_Y \times Z_2$ symmetry in this model. Here $M_L = (\nu_L, \mu_L^-)$ is the second generation of the lepton doublet and $\Psi = (\psi^0, \psi^-)$.

Given the motivations mentioned above, there is an active demand for a model that can address these issues. We propose a simple DM model that extends the SM by introducing singlet and doublet Dirac fermion fields, along with a doublet complex scalar field. This model is designed to explain the $(g-2)_\mu$, the CDF M_W , as well as the GCE and AMS-02 \bar{p} excesses. We find the feasible parameter regions have the following intriguing features: (i) The mass of the scalar DM candidate is favored to lie within the range of 53 to 74 GeV. If the W boson mass is consistent with the electroweak fit results, a DM mass heavier than 500 GeV is still allowed. (ii) The compressed mass spectrum in the inert scalar sector is strongly constrained by current and upcoming LHC searches. (iii) The current constraints from the DM direct detection at LZ experiment already excluded a significant portion of the parameter space for the Higgs resonance. (iv) The neutral particles in the leptophilic fermion sector are difficult to explore at the LHC; however, a high-energy muon collider could be an ideal machine for detecting them and testing the predictions of this model.

The structure of this paper is organized as follows. We first introduce our simple DM model in Sec. II. We then discuss the extra $(g-2)_\mu$ and M_W contributions, as well as the constraints in this model in Sec. III. Our main results are presented in Sec. IV. Finally, we conclude our findings in Sec. V.

II. THE MODEL

The SM is extended by introducing singlet and doublet Dirac fermion fields (χ and Ψ) as well as a doublet complex scalar field (H_2). To ensure the stability of the DM candidate, we impose a Z_2 symmetry on the model and assume that all new fields (SM fields) are Z_2 odd (even). The relevant fields under the $SU(2)_L \times U(1)_Y \times Z_2$ symmetry in this model are shown in Table I, where H_1 represents the SM scalar doublet, $M_L = (\nu_L, \mu_L^-)$ is the second generation of the lepton doublet, and $\Psi = (\psi^0, \psi^-)$. The renormalizable Lagrangian involving these new fields can be written as

$$\mathcal{L} = \mathcal{L}_F + \mathcal{L}_S + \mathcal{L}_{\text{mix}}, \quad (1)$$

where

$$\mathcal{L}_F = \bar{\Psi} (\not{D} - M_\Psi) \Psi + \bar{\chi} (\not{\partial} - M_\chi) \chi + (y_{H_1} \bar{\chi} \Psi \cdot H_1 + h.c.), \quad (2)$$

$$\begin{aligned} \mathcal{L}_S = & |D_\mu H_1|^2 + |D_\mu H_2|^2 - \mu_1^2 |H_1|^2 - \mu_2^2 |H_2|^2 - \lambda_1 |H_1|^4 - \lambda_2 |H_2|^4 \\ & - \lambda_3 |H_1|^2 |H_2|^2 - \lambda_4 (H_1^\dagger H_2) (H_2^\dagger H_1) - \frac{\lambda_5}{2} \left[(H_1^\dagger H_2)^2 + h.c. \right], \end{aligned} \quad (3)$$

$$\mathcal{L}_{\text{mix}} = \kappa_M \bar{\chi} M_L \cdot H_2 + \kappa_\mu \bar{\Psi} \mu_R H_2 + h.c.. \quad (4)$$

Here D_μ is the covariant derivative in the SM, and the $SU(2)_L$ contraction $\Psi \cdot H_\alpha = \epsilon_{ab} \Psi_a H_{\alpha b}$ with $\epsilon_{ab} = (i\sigma_2)_{ab}$ and $\alpha = 1, 2$. Note that M_Ψ , M_χ , μ_i ($i = 1, 2$) are parameters with the same dimension as mass and y_{H_1} , λ_i ($i = 1 - 5$), κ_M , κ_μ are dimensionless parameters. Furthermore, we assume all dimensionless parameters are real in this work.

Some comments on this model are as follows:

- The inclusion of the third term in Eq. (2) aims to generate the chiral enhancement effect in the one-loop process to Δa_μ . Without the presence of this chiral enhancement effect, it becomes challenging for the vector-like leptons to provide a simultaneous explanation for Δa_μ and to satisfy the collider constraints [24].

- Both the doublets H_2 and Ψ can contribute to the oblique parameters, S , T , and U [25], thereby alleviating the strong restrictions on the parameter space of the inert 2HDM [26].
- The singlet fermion field χ cannot be a Majorana type as it would lead to excessively large neutrino masses via the one-loop process [27] in our parameter space of interest.
- \mathcal{L}_F or \mathcal{L}_S alone can represent a Lagrangian for a pure fermion or scalar DM model. However, neither by itself can provide a significant contribution to Δa_μ . Therefore, we combine both of them with \mathcal{L}_{mix} in this work.
- We only consider the second generation of the lepton sector in \mathcal{L}_{mix} for simplicity, but it can be straightforwardly extended to include all three generations of the lepton sector.

After electroweak symmetry breaking (EWSB), the masses of scalar fields can be represented as

$$\begin{aligned}
m_h^2 &= -2\mu_1^2 = 2\lambda_1 v^2, \\
m_S^2 &= \mu_2^2 + \frac{1}{2}(\lambda_3 + \lambda_4 + \lambda_5)v^2, \\
m_A^2 &= \mu_2^2 + \frac{1}{2}(\lambda_3 + \lambda_4 - \lambda_5)v^2, \\
m_{H^\pm}^2 &= \mu_2^2 + \frac{1}{2}\lambda_3 v^2,
\end{aligned}$$

and the mass matrix of singlet-doublet fermion fields is

$$\begin{pmatrix} M_\chi & y_{H_1} v / \sqrt{2} \\ y_{H_1} v / \sqrt{2} & M_\Psi \end{pmatrix}. \quad (5)$$

Similarly, after EWSB, the neutral components χ and ψ^0 mix giving the mass eigenstates n_1, n_2 ,

$$\begin{pmatrix} \chi \\ \psi^0 \end{pmatrix} = \begin{pmatrix} \cos \alpha & -\sin \alpha \\ \sin \alpha & \cos \alpha \end{pmatrix} \begin{pmatrix} n_1 \\ n_2 \end{pmatrix}, \quad (6)$$

with mass eigenvalues

$$m_{n_1, n_2} = \frac{1}{2} \left(M_\Psi + M_\chi \mp \sqrt{(M_\Psi - M_\chi)^2 + 2y_{H_1}^2 v^2} \right), \quad (7)$$

and the rotation angle α is

$$\sin 2\alpha = \frac{\sqrt{2}y_{H_1}v}{m_{n_2} - m_{n_1}}. \quad (8)$$

We assume that n_2 is heavier than n_1 . Finally, the mass of charged fermion ψ^\pm in the doublet field can be given as $m_{\psi^\pm} = M_\Psi$. We take $m_h = 125$ GeV and $v = 246$ GeV to eliminate μ_1 and λ_1 , so there are ten free parameters in this model left. Besides, as λ_2 primarily influences the self-interactions of inert scalars and loop corrections [28–31], neither of which significantly impacts the main findings of this study, we can conveniently assign $\lambda_2 = 10^{-2}$.

Subsequently, we introduce several key parameters in our analysis: the neutral mass splitting, Δ^0 , the charged mass splitting, Δ^\pm , the coupling λ_S between h and a pair of S , and the disparity between two fermion mass parameters, $\Delta_{\Psi\chi}$ in the following:

$$\begin{aligned} \Delta^0 &= m_A - m_S, \\ \Delta^\pm &= m_{H^\pm} - m_S, \\ \lambda_S &= (\lambda_3 + \lambda_4 + \lambda_5) / 2, \\ \Delta_{\Psi\chi} &= M_\Psi - M_\chi. \end{aligned}$$

Utilizing the definitions provided above, we establish the scanning intervals for the nine free model parameters as follows:

$$\begin{aligned} 30 &\leq m_S/\text{GeV} \leq 100, \\ 10^{-3} &\leq \Delta^0/\text{GeV} \leq 500, \\ 1 &\leq \Delta^\pm/\text{GeV} \leq 500, \\ -1.0 &\leq \lambda_S \leq 1.0, \\ -\sqrt{4\pi} &< y_{H_1} < \sqrt{4\pi}, \\ -\sqrt{4\pi} &< \kappa_M < \sqrt{4\pi}, \\ -\sqrt{4\pi} &< \kappa_\mu < \sqrt{4\pi}, \\ 600 &\leq M_\Psi/\text{GeV} \leq 1500, \\ 1 &\leq \Delta_{\Psi\chi}/\text{GeV} \leq 500. \end{aligned}$$

Here we impose the stipulation that S as the DM candidate, ensuring that $m_S < m_{n_1, n_2}$. Therefore, $m_{n_1} > 100$ GeV is required in our scanning. The selection of the scanning ranges for m_S , Δ^0 , Δ^\pm , and λ_S adheres to the guidelines outlined in our previous investigations [26,

31]. Additionally, for perturbative consistency, we enforce the bounds $|y_{H_1}|$, $|\kappa_M|$, and $|\kappa_\mu|$ to be less than $\sqrt{4\pi}$. Furthermore, to evade the constraints imposed by ATLAS and CMS slepton searches [32, 33], we conservatively require the condition $M_\Psi > 600$ GeV.

III. THE EXTRA $(g-2)_\mu$, M_W CONTRIBUTIONS AND OTHER CONSTRAINTS

In this section, we will initially delve into the manner in which our model contributes to Δa_μ and M_W , as outlined in Sec. III A. Subsequently, we will provide an overview of the relevant theoretical and experimental constraints in Sec. III B.

A. Contributions to Δa_μ and M_W

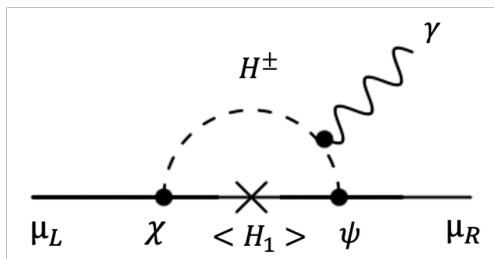


FIG. 1: The one-loop chirally enhanced Feynman diagram to the Δa_μ in this model.

The dominant contribution to Δa_μ in this model arises from the one-loop chirally enhanced Feynman diagram depicted in Fig. 1. This contribution can be expressed in the form [34, 35]:

$$\Delta a_\mu \simeq -\frac{\kappa_M \kappa_\mu m_\mu}{4\pi^2 m_{H^\pm}^2} \sin 2\alpha \left[m_{n_1} \tilde{H}(x_1) - m_{n_2} \tilde{H}(x_2) \right], \quad (9)$$

where $x_i = (m_{n_i}/m_{H^\pm})^2$ and $\tilde{H}(x) = (x^2 - 1 - 2x \log x) / [8(x - 1)^3]$. Due to the effect of chiral enhancement, Δa_μ is proportionate to m_{n_1, n_2} . In Fig. 2, we show contours of Δa_μ spanned in the (m_Ψ, m_{H^\pm}) plane. Here we fixed values of $\Delta M_{\Psi\chi} = 100$ GeV, $|y_{H_1}| = 1$, and $|\kappa_M \times \kappa_\mu| = 0.5$. To achieve a positive and substantial Δa_μ from Eq. (9), one possible scenario involves $\kappa_M \times \kappa_\mu \times y_{H_1} < 0$ and $m_{H^\pm} \ll m_{n_2}$ as shown in the left panel of Fig. 2. When $\kappa_M \times \kappa_\mu \times y_{H_1} > 0$, the sign of Δa_μ flips, as shown in the right panel of Fig. 2. In this case, the region favored by the discrepancy in Δa_μ (orange band) is already excluded by the LHC constraints on Ψ mass, i.e $m_\Psi > 600$ GeV.

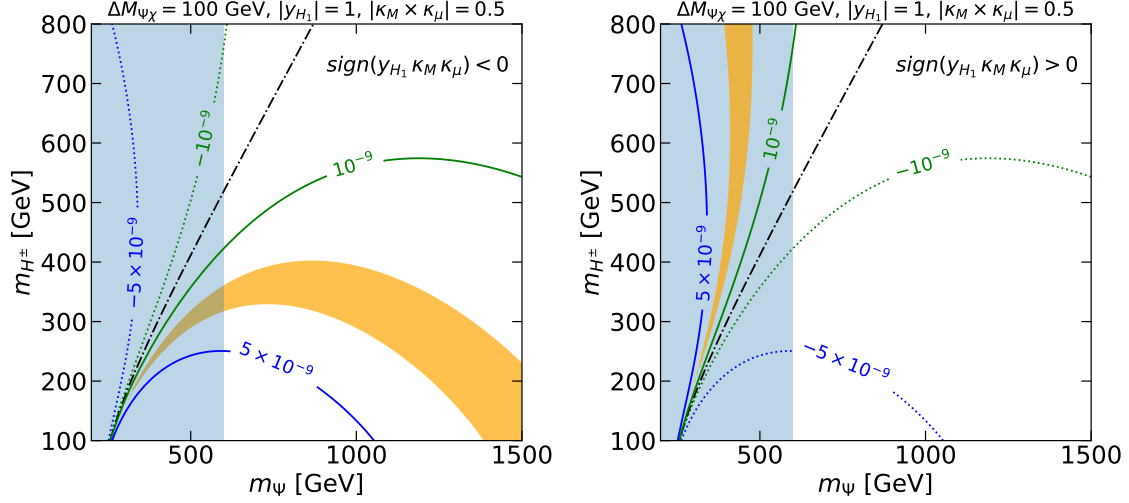


FIG. 2: The contribution to Δa_μ in this model on the (m_Ψ, m_{H^\pm}) plane. We fixed $\Delta M_{\Psi\chi} = 100$ GeV, $|y_{H_1}| = 1$ and $|\kappa_M \times \kappa_\mu| = 0.5$. The sign of $y_{H_1} \kappa_M \kappa_\mu$ is fixed to be negative in the left panel while it is positive in the right panel. The solid blue, green, dotted blue and green represent the values of Δa_μ of 5×10^{-9} , 10^{-9} , -10^{-9} and -5×10^{-9} , respectively. The dash-dotted black line indicates $\Delta a_\mu = 0$, where a complete cancellation between the two terms in the brackets of Eq. 9 occurs. The orange band is the 1σ region favored to the discrepancy between the current experiment measurements and the SM results where the HVP is calculated using the data-driven method [2]. The light blue region is excluded by the LHC constraints.

We note that the contributions from other subdominant terms to Δa_μ are notably smaller than the one mentioned above, we have omitted their contributions in this study [34, 36]. On the other hand, the contributions solely from the charged scalar to Δa_μ are negative and negligible as the situation in the inert two Higgs doublet model, thus we can disregard them.

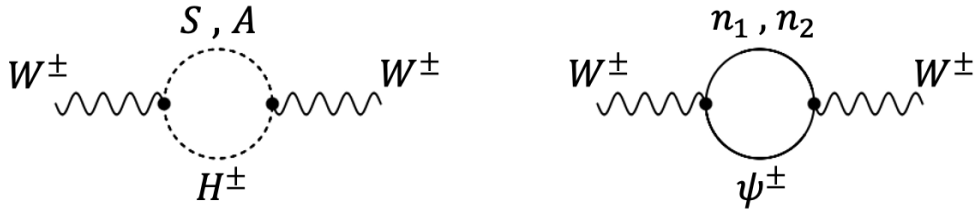


FIG. 3: The Feynman diagrams for the one-loop W boson mass corrections with the inert Higgs sector and new Dirac fermions.

Except for the contributions to Δa_μ , this model can also provide corrections to the squared W boson mass. In Fig. 3, we show two representative Feynman diagrams which can contribute to m_W in this model. Generally, Δm_W^2 can be expressed in terms of the oblique parameters \mathcal{S} , \mathcal{T} , and \mathcal{U} [25] as

$$\Delta m_W^2 = \frac{\alpha_{\text{EM}} c_W^2 m_Z^2}{c_W^2 - s_W^2} \left[-\frac{\mathcal{S}}{2} + c_W^2 \mathcal{T} + \frac{c_W^2 - s_W^2}{4s_W^2} \mathcal{U} \right], \quad (10)$$

where c_W (s_W) is the cosine (sine) of the weak mixing angle, the fine structure constant is denoted as α_{EM} , and the Z boson mass is represented as m_Z . Since the contributions of new physics to the \mathcal{U} parameter are often higher-order corrections and much more suppressed compared to the contributions from the \mathcal{S} and \mathcal{T} parameters, for the sake of simplicity, we typically ignore the contributions from the \mathcal{U} parameter.

In addition to the higher-order contributions from the SM to Δm_W^2 , there are two extra contributions to Δm_W^2 in this model. The first contributions to Δm_W^2 in this model come from the inert Higgs doublet sector, and the contributions to \mathcal{S} and \mathcal{T} can be represented as [37–39]:

$$\mathcal{S} = \frac{1}{2\pi} \left[\frac{1}{6} \ln \left(\frac{m_S^2}{m_{H^\pm}^2} \right) - \frac{5}{36} + \frac{m_S^2 m_A^2}{3(m_A^2 - m_S^2)^2} + \frac{m_A^4 (m_A^2 - 3m_S^2)}{6(m_A^2 - m_S^2)^3} \ln \left(\frac{m_A^2}{m_S^2} \right) \right], \quad (11)$$

and

$$\mathcal{T} = \frac{1}{32\pi^2 \alpha_{\text{EM}} v^2} [F(m_h, m_A) + F(m_h, m_S) - F(m_A, m_S)], \quad (12)$$

where

$$F(M_a, M_b) = \frac{M_a^2 + M_b^2}{2} - \frac{M_a^2 M_b^2}{M_a^2 - M_b^2} \ln \frac{M_a^2}{M_b^2}. \quad (13)$$

We use the 2HDMC [40] to calculate the \mathcal{S} and \mathcal{T} parameters from the inert Higgs doublet sector. We observe that if $m_{H^\pm} < m_A$, a positive value of \mathcal{S} is generated, resulting in reduced corrections to Δm_W^2 . Consequently, there is a preference for the charged Higgs boson to be the heaviest within the inert Higgs doublet sector when a larger m_W is needed. On the other hand, the generation of a positive \mathcal{T} is favored with a large Δ^\pm and/or $\Delta^\pm - \Delta^0$, leading to an increase in Δm_W^2 .

The second contributions to Δm_W^2 in this model come from the Ψ field, and these addi-

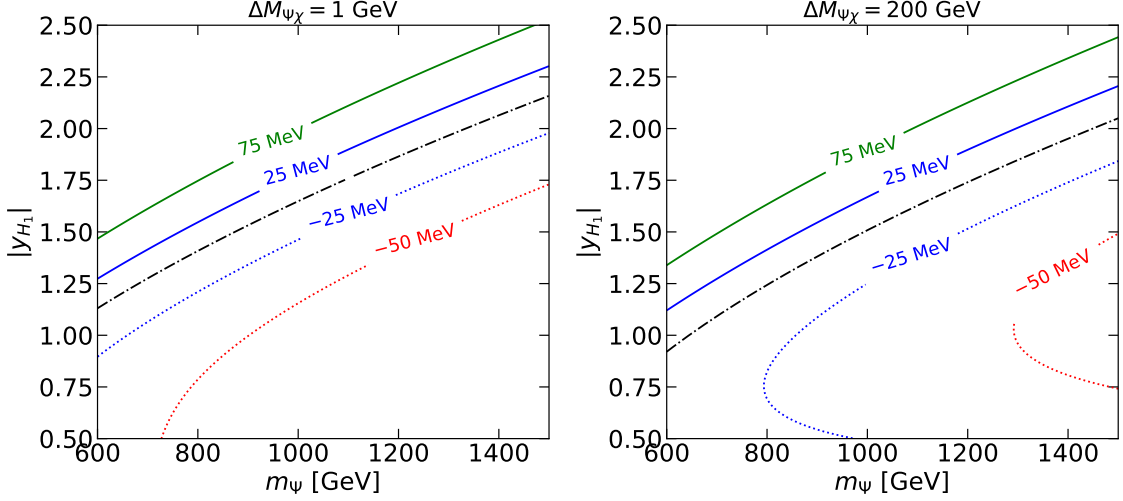


FIG. 4: Contribution to Δm_W from the Ψ field projected onto the $(m_\Psi, |y_{H_1}|)$ plane. In the left panel, we fixed $\Delta M_{\Psi\chi} = 1$ GeV, while in the right panel, $\Delta M_{\Psi\chi} = 200$ GeV. The dotted red, dotted blue, solid blue and solid green lines represent the values of Δm_W equal to -50 MeV, -25 MeV, 25 MeV, and 75 MeV, respectively. The dash-dotted black line indicates $\Delta m_W = 0.0$.

tional contributions to the \mathcal{S} and \mathcal{T} parameters can be summarized as follows [41, 42]:

$$\begin{aligned} \mathcal{S} = & \frac{g^2 s_W^2 c_W^2}{4\pi^2 \alpha_{\text{EM}}} \left[\frac{1}{3} \left\{ \ln \left(\frac{\Lambda_{\text{EW}}^2}{m_{\psi^\pm}^2} \right) - \cos^4 \alpha \ln \left(\frac{\Lambda_{\text{EW}}^2}{m_{n_2}^2} \right) - \sin^4 \alpha \ln \left(\frac{\Lambda_{\text{EW}}^2}{m_{n_1}^2} \right) \right\} - \frac{1}{2} \sin^2 2\alpha \left\{ \ln \left(\frac{\Lambda_{\text{EW}}^2}{m_{n_1} m_{n_2}} \right) \right. \right. \\ & + \frac{m_{n_1}^4 - 8m_{n_1}^2 m_{n_2}^2 + m_{n_2}^4}{9(m_{n_1}^2 - m_{n_2}^2)^2} + \frac{(m_{n_1}^2 + m_{n_2}^2)(m_{n_1}^4 - 4m_{n_1}^2 m_{n_2}^2 + m_{n_2}^4)}{6(m_{n_1}^2 - m_{n_2}^2)^3} \ln \left(\frac{m_{n_2}^2}{m_{n_1}^2} \right) \\ & \left. \left. + \frac{m_{n_1} m_{n_2} (m_{n_1}^2 + m_{n_2}^2)}{2(m_{n_1}^2 - m_{n_2}^2)^2} + \frac{m_{n_1}^3 m_{n_2}^3}{(m_{n_1}^2 - m_{n_2}^2)^3} \ln \left(\frac{m_{n_2}^2}{m_{n_1}^2} \right) \right\} \right], \end{aligned} \quad (14)$$

and

$$\mathcal{T} = \frac{g^2}{16\pi^2 \alpha_{\text{EM}} M_W^2} \left[\frac{1}{2} \sin^2 2\alpha \Pi'(m_{n_1}, m_{n_2}, 0) - 2 \cos^2 \alpha \Pi'(m_{\psi^\pm}, m_{n_2}, 0) - 2 \sin^2 \alpha \Pi'(m_{\psi^\pm}, m_{n_1}, 0) \right], \quad (15)$$

where $\Pi'(M_a, M_b, 0)$ is given by

$$\begin{aligned} \Pi'(M_a, M_b, 0) = & -\frac{1}{2}(M_a^2 + M_b^2) \ln \left(\frac{\Lambda_{\text{EW}}^2}{M_a M_b} \right) - \frac{1}{4}(M_a^2 + M_b^2) - \frac{(M_a^4 + M_b^4)}{4(M_a^2 - M_b^2)} \ln \frac{M_b^2}{M_a^2} \\ & + M_a M_b \left\{ \ln \left(\frac{\Lambda_{\text{EW}}^2}{M_a M_b} \right) + 1 + \frac{(M_a^2 + M_b^2)}{2(M_a^2 - M_b^2)} \ln \frac{M_b^2}{M_a^2} \right\}. \end{aligned} \quad (16)$$

Here Λ_{EW} is at the electroweak scale and we set $\Lambda_{\text{EW}} = 246$ GeV.

To investigate the influence of the model parameters m_Ψ , y_{H_1} , and $\Delta M_{\Psi\chi}$ on Δm_W , we analyze the impact of the Ψ field on Δm_W in the $(m_\Psi, |y_{H_1}|)$ plane. The results are presented in Fig. 4 for two cases: $\Delta M_{\Psi\chi} = 1$ GeV (left panel) and $\Delta M_{\Psi\chi} = 200$ GeV (right panel). The presence of Ψ field can significantly affect the mass of the W boson. In particular, the W boson mass increases as $|y_{H_1}|$ becomes larger. Additionally, smaller masses of Ψ and χ , result in a further increase in the W boson mass. In certain specific regions, the effect from the Ψ field can even dominate the contributions from the inert Higgs doublet sector. For instance, at $\Delta M_{\Psi\chi} = 1$ GeV, $m_\Psi = 1$ TeV and $|y_{H_1}| = 2$, the resulting $\Delta m_W \sim 75$ MeV, consistent with the CDF II measurement. Nevertheless, it is important to note that in certain areas of the parameter space, the contribution to Δm_W diminishes, as depicted by the dash-dotted black line in Fig. 4.

B. Theoretical and experimental constraints

The relevant constraints for this model can be categorized into theoretical and experimental aspects. Regarding the theoretical constraints, we incorporate considerations of perturbativity, stability, and tree-level unitarity in the scalar sector, all of which are implemented using the 2HDMC. As for the experimental constraints, we outline them as follows:

- Production of inert scalars at the LEP

Firstly, it's important to note that no signals have been reported by LEP for processes like $W^\pm \rightarrow (SH^\pm, AH^\pm)$, and $Z \rightarrow (SA, H^+H^-)$ [43]. This leads to conditions such as $m_{S,A} + m_{H^\pm} > m_W$, $m_A + m_S > m_Z$, and $2m_{H^\pm} > m_Z$. For the heavier inert scalars, they can also be directly produced from processes like $e^+e^- \rightarrow SA$ and $e^+e^- \rightarrow H^+H^-$. We closely follow the strategies outlined in Refs. [31, 44, 45] to recast the constraints based on searches conducted by the OPAL collaboration [46].

- Higgs boson invisible and exotic decays

When the inert scalars have masses lower than half of m_h , certain decay modes become kinematically possible. These include the Higgs invisible decay, $h \rightarrow SS$, and the Higgs exotic decays, $h \rightarrow AA, H^+H^-$ ¹. In our analysis, we consider $\text{BR}(h \rightarrow \text{invisible}) < 10.7\%$ [48] and $\text{BR}(h \rightarrow \text{undetected}) < 19\%$ [49] at 95% C.L.

¹ Given that the soft visible objects cannot be identified at the LHC, we classify $h \rightarrow AA, H^+H^-$ as Higgs invisible decays when $\Delta^{0,\pm}$ is less than about 2 GeV [47].

- The $h \rightarrow \gamma\gamma$ signal strength

If the newly introduced charged particles can interact with the Higgs boson, the $h \rightarrow \gamma\gamma$ signal strength measurements can indirectly impose constraints on them. The $h \rightarrow \gamma\gamma$ signal strength measurements from the ATLAS (CMS) collaborations are reported as follows [50, 51]:

$$\mu_{\gamma\gamma} = 1.04_{-0.09}^{+0.10}(1.12 \pm 0.09). \quad (17)$$

In this model, only H^\pm can contribute to the $h \rightarrow \gamma\gamma$ process [52].

- Mono-jet and compressed mass spectra searches at the LHC

A common approach for searching for DM at the LHC involves investigating final states characterized by significant missing transverse energy associated with visible particles. In this model, the mono-jet signal comprises a pair of S particles originating from the Higgs boson, a $n_1\bar{n}_1$ pair originating from the Z and Higgs bosons, and then $n_1 \rightarrow \nu_\mu S$ and $\bar{n}_1 \rightarrow \bar{\nu}_\mu S$, accompanied by at least one high-energy jet. Similarly, if the mass difference between A and S is sufficiently small, a pair of A particles produced through Higgs boson or SA production via the Z boson can contribute to the mono-jet signature. On the other hand, when the mass splittings (Δ^0 and/or Δ^\pm) are not large enough, searches focusing on compressed mass spectra become pivotal. In this model, compressed mass spectra searches can be performed for pairs of SA , AH^\pm , and H^+H^- , generated through $q\bar{q}$ fusion and VBF processes as well as $pp \rightarrow n_1\bar{n}_1$ with $n_1 \rightarrow \nu_\mu S, \nu_\mu A, \mu^- H^+$ and $\bar{n}_1 \rightarrow \bar{\nu}_\mu S, \bar{\nu}_\mu A, \mu^+ H^-$ at the LHC. We reanalyze the current ATLAS mono-jet search [53] and SUSY compressed mass spectra search [54] using Madgraph 5 [55], Pythia8 [56], Delphes3 [57] and Madanalysis 5 [58], as described in more detail in Ref. [31]. Please note that in the upcoming section, we will demonstrate that n_2 and ψ^\pm are sufficiently heavy to evade constraints from the current LHC data.

- DM relic density

The dominant channels for DM annihilation in this model depend on the specific mass spectrum. In the Higgs resonance regions where $m_S \simeq m_h/2$, the annihilation process $SS \rightarrow b\bar{b}$ mediated by the Higgs boson exchange prevails. In the region where $m_S > m_h/2$, the dominant annihilation channels are $SS \rightarrow W^+W^{-(*)}$, involving in-

interactions through a four-vertex interaction, s -channel Higgs boson exchange, and t -channel H^\pm exchange. Additionally, co-annihilation processes play a role, such as $SA \rightarrow f\bar{f}$ for small Δ^0 and $SH^\pm \rightarrow \gamma W^\pm$ for small Δ^\pm . Beyond these DM annihilation or co-annihilation channels found in the inert 2HDM, there are also new annihilation channels of $SS \rightarrow \mu^+\mu^-$ via the t -channel ψ^\pm exchange and $SS \rightarrow \nu\bar{\nu}$ via the t -channel n_1, n_2 exchange. To quantify these processes, we numerically solve the Boltzmann equation using `micrOMEGAs` [59], accounting for all possible annihilation and co-annihilation contributions. The relic density of DM is required to align with the PLANCK measurement [60]:

$$\Omega_{\text{DM}}h^2 = 0.1198 \pm 0.0015. \quad (18)$$

- DM direct detection

The null signals from DM direct detection experiments have placed stringent constraints on the scattering cross section between DM and nuclei. For instance, the spin-independent DM-nuclear scattering cross section has been excluded above 9.2×10^{-48} cm² for a DM mass of 36 GeV at the 90% confidence level from the current LZ experiment [13]. In this model, the leading-order contributions to DM-nuclear scattering originate from DM-quark/gluon elastic scattering mediated by the exchange of a Higgs boson in the t -channel. We utilize `micrOMEGAs` to compute the spin-independent DM-nucleon scattering cross section.

IV. RESULTS AND DISCUSSIONS

A. Methodology

We employ the “*Profile Likelihood*” method [66] to eliminate nuisance parameters and illustrate the two dimensional contours. The specific experimental constraints are listed in Table II. First of all, we use the theoretical bounds as well as LEP-II and OPAL limits as the hard cuts. Secondly, for Gaussian functions, we employ the following chi-square equation:

$$\chi^2 = \left(\frac{\mu - \mu_{\text{exp}}}{\sigma} \right)^2 \quad \text{and} \quad \sigma = \sqrt{\sigma_{\text{theo}}^2 + \sigma_{\text{exp}}^2}, \quad (19)$$

where μ represents the theoretical prediction and μ_{exp} denotes the experimental central value. However, for Half-Gaussian functions where a null signal is expected, we set $\mu_{\text{exp}} = 0$.

Likelihood type	Constraints
Step	perturbativity, stability, unitarity [40]
Step	LEP-II [61], OPAL [62]
Half-Gaussian	current-LZ [13]
Half-Gaussian	Higgs invisible decays [48]
Half-Gaussian	Higgs exotic decays [49]
Gaussian	relic abundance [63]
Gaussian	$R_{\gamma\gamma}$ [64]
Gaussian	$m_{W,\text{CDF II}}$ [4] or $m_{W,\text{PDG}}$ [65]
Gaussian	$\Delta a_{\mu}^{e^+e^- \text{ HVP}}$ [2] or $\Delta a_{\mu}^{\text{Lattice HVP}}$ [3]

TABLE II: Likelihood distributions and constraints used in our analysis.

The uncertainty σ incorporates both theoretical and experimental errors. By summing the individual χ^2 of these constraints, we obtain the total χ_{tot}^2 as

$$\chi_{\text{tot}}^2 = \chi_{a_{\mu}}^2 + \chi_{m_W}^2 + \chi_{\Omega h^2}^2 + \chi_{\text{hexo}}^2 + \chi_{\text{hinv}}^2 + \chi_{R_{\gamma\gamma}}^2 + \chi_{\text{LZ}}^2, \quad (20)$$

where $\chi_{a_{\mu}}^2$, $\chi_{m_W}^2$, $\chi_{\Omega h^2}^2$, χ_{hexo}^2 , χ_{hinv}^2 , $\chi_{R_{\gamma\gamma}}^2$ and χ_{LZ}^2 represent the χ^2 from muon $g-2$, W -boson mass, DM relic density, Higgs boson exotic decays, Higgs boson invisible decays, signal strength of Higgs boson to diphoton and DM direct detection, respectively.

To elucidate the effects of quality anomalies from muon $g-2$ and W -boson mass, we conduct four sets of numerical scans:

1. $m_{W,\text{CDF II}} = 80.4335 \pm 0.0094$ GeV and $\Delta a_{\mu}^{e^+e^- \text{ HVP}} = 249(48) \times 10^{-11}$;
2. $m_{W,\text{PDG}} = 80.377 \pm 0.012$ GeV and $\Delta a_{\mu}^{e^+e^- \text{ HVP}} = 249(48) \times 10^{-11}$;
3. $m_{W,\text{CDF II}} = 80.4335 \pm 0.0094$ GeV and $\Delta a_{\mu}^{\text{Lattice HVP}} = 105(59) \times 10^{-11}$;
4. $m_{W,\text{PDG}} = 80.377 \pm 0.012$ GeV and $\Delta a_{\mu}^{\text{Lattice HVP}} = 105(59) \times 10^{-11}$.

Here $m_{W,\text{CDF II}}$ and $m_{W,\text{PDG}}$ are the W boson mass results from the CDF II experiments and from the Particle Data Group [65], respectively. The muon $g-2$ results, $\Delta a_{\mu}^{e^+e^- \text{ HVP}}$ and $\Delta a_{\mu}^{\text{Lattice HVP}}$, correspond to the HVP contributions obtained via data-driven and lattice calculation methods, respectively.

On the other hand, we also compare our allowed parameter space with several DM indirect detection constraints. These include the bounds established by the Fermi LAT observations of dwarf Spheroidal galaxies [67], the signal regions of the Fermi LAT Galactic Center γ -ray excess [16–19], and the Alpha Magnetic Spectrometer AMS-02 experiment antiproton excess [68–71].

We conduct Markov Chain Monte Carlo (MCMC) scans using the EMCEE [72] code and obtain around $\mathcal{O}(4.5 \times 10^6)$ data points. The confidence intervals are derived from the tabulated values of $\Delta\chi^2 \equiv -2\ln(\mathcal{L}/\mathcal{L}_{\max})$ where \mathcal{L}_{\max} is the likelihood at the best-fits. For a two-dimensional plot, the 95% confidence level (C.L.) region (2σ allowed region) is defined as $\Delta\chi^2 \leq 5.99$, assuming an approximate Gaussian likelihood.

B. Results

In this section, we present the 95% C.L. regions for the total likelihoods, as shown in Table II. Unless otherwise specified, the gray circles and red hollow diamonds represent scenarios where the model parameter regions favor $m_{W,\text{PDG}} + \Delta a_\mu^{\text{Lattice HVP}}$ and $m_{W,\text{CDF II}} + \Delta a_\mu^{e^+e^- \text{HVP}}$, respectively.

Within the range of model parameters we consider, the DM mass m_S is found to lie between 54 and 74 GeV, irrespective of whether the anomalies in the muon magnetic moment and the W boson mass are taken into account. In the upper left panel of Fig. 5, we show the 95% C.L. region for m_S and Δ^0 . The DM mass clearly falls into three distinct regions, each corresponding to a different dominant DM annihilation mechanism in the early universe. For $m_S \approx m_h/2$, this corresponds to the Higgs resonance. The $\Delta^0 \lesssim 10$ GeV indicates SA co-annihilation, while $71 \lesssim m_S \lesssim 74$ GeV corresponds to the $SS \rightarrow WW^*$ process. The gray region contains a few scattered points, which arise from DM annihilation processes dominated by neutrino final states via the exchange of $n_{1,2}$. However, the significant overlap between the gray and red regions suggests that the anomalies in the muon magnetic moment and the W boson mass have only a slight effect on the dominant DM annihilation mechanisms.

For the SA co-annihilation mechanism, we present an enlarged view of the 95% C.L. regions for m_S versus Δ^0 in the upper right panel of Fig. 5. The solid black line represents the exclusion limits from the CMS search for two or three soft leptons at the 13 TeV LHC, with

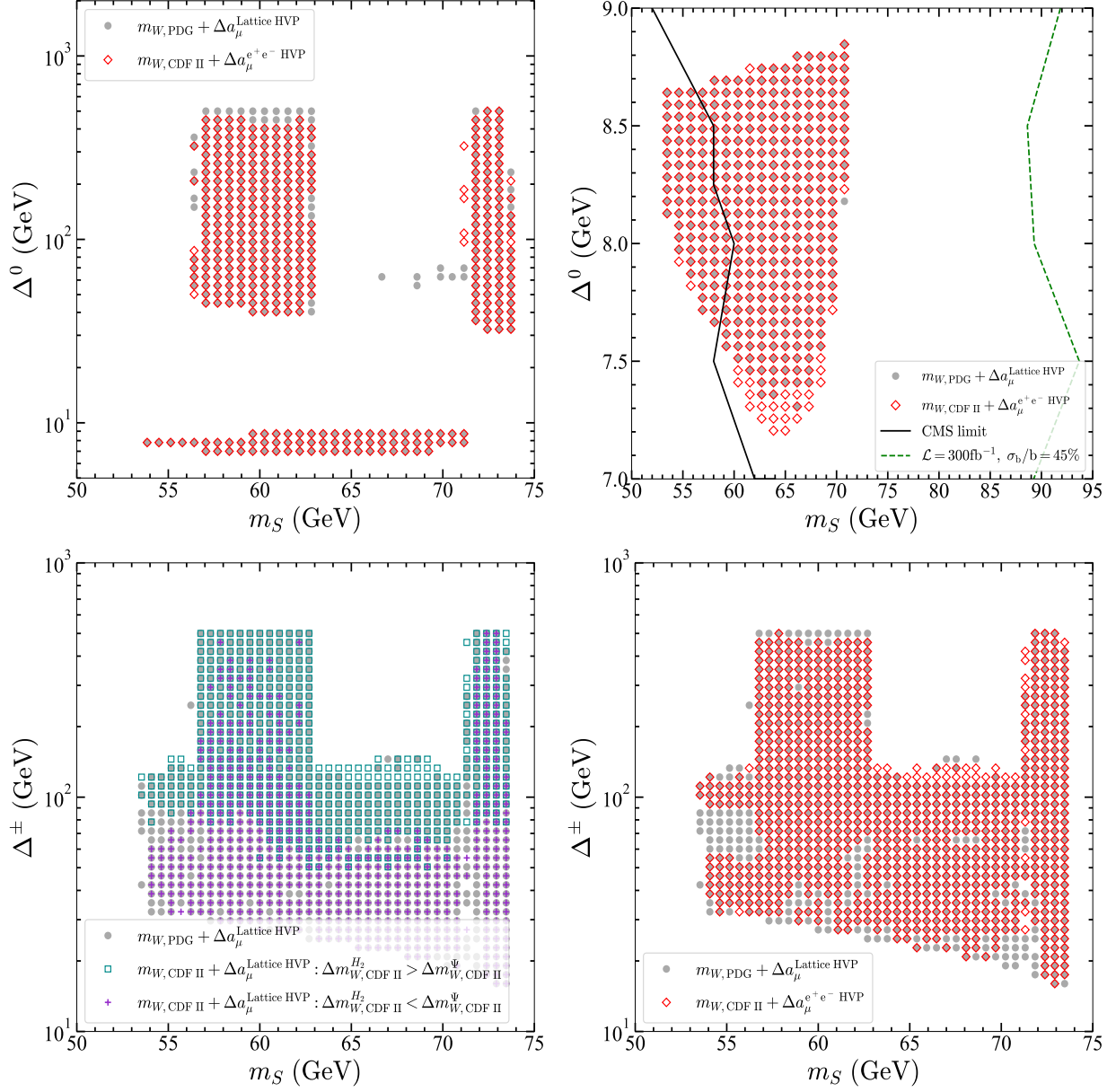


FIG. 5: The 95% C.L. regions on the panels of m_s versus Δ^0 (upper panels) and Δ^\pm (lower panels). The gray region favored by the data of $m_{W,\text{PDG}}$ and $\Delta a_\mu^{\text{Lattice HVP}}$. The red diamond region represents the combined results of $m_{W,\text{CDF II}}$ and $\Delta a_\mu^{e^+e^- \text{ HVP}}$. The green box indicates the region where the contribution to $m_{W,\text{CDF II}}$ satisfies $\Delta m_{W,\text{CDF II}}^{H_2} > \Delta m_{W,\text{CDF II}}^\Psi$, while the purple cross represents the region where $\Delta m_{W,\text{CDF II}}^{H_2} < \Delta m_{W,\text{CDF II}}^\Psi$. The solid black and dashed green lines in the upper right panel indicate the current limit from CMS and future probe from LHC Run 3, respectively.

an integrated luminosity of 137 fb^{-1} [54]. The green dashed line illustrates the projected 2σ sensitivity, assuming a conservative background uncertainty of $\sigma_b/b = 45\%$, for an integrated luminosity of 300 fb^{-1} in one of the signal regions. With the forthcoming LHC luminosity upgrades, the entire SA coannihilation region is expected to be thoroughly tested. Detailed calculations and discussions regarding collider experiments can be found in the latter part of this section and in Sec. IV C.

After imposing all constraints, Δ^\pm is limited to the range of $17\text{--}500 \text{ GeV}$ for the $m_{W,\text{PDG}} + \Delta a_\mu^{\text{Lattice HVP}}$ scenario, as shown by the gray regions in the lower panels of Fig. 5. In this model, the extra corrections to W boson mass arise from loop contributions involving the inert Higgs fields H_2 and new fermion fields Ψ (as depicted in Fig. 3). If the H_2 sector serves as the dominant contribution, an larger mass splitting between the charged Higgs H^\pm and the neutral Higgs S is expected. In a more conservative scenario, we require the $\Delta m_{W,\text{CDF II}}^{H_2} > \Delta m_{W,\text{CDF II}}^\Psi$, which corresponds to the green box regions in the lower left panel of Fig. 5. However, if $m_{W,\text{CDF II}}$ is primarily influenced by corrections from the Ψ fields, the heavy charge Higgs H^\pm becomes unnecessary. In this case, we impose $\Delta m_{W,\text{CDF II}}^{H_2} < \Delta m_{W,\text{CDF II}}^\Psi$, with the allowed regions denoted by purple crosses. Clearly, compared to the scenario dominated by the inert Higgs, the 95% C.L. regions for Δ^\pm shift downward. Finally, we present results that jointly consider both $m_{W,\text{CDF II}}$ and $\Delta a_\mu^{e^+e^- \text{ HVP}}$, shown as red diamond regions in the lower right panel of Fig. 5. Clearly, the constraint results are not more stringent than the those in the gray regions. This model relaxes the requirement for a larger Δ^\pm contribution to $m_{W,\text{CDF II}}$ compared to the traditional inert 2HDM.

In the left panel of Fig. 6, we present the 95% C.L. regions for the Higgs-DM-DM coupling λ_S as a function of the DM mass. We find that λ_S must remain small, mainly due to the Planck relic density constraint, as a larger coupling leads to an overabundance of DM. As expected, the viable range of λ_S is not significantly affected when the $m_{W,\text{PDG}} + \Delta a_\mu^{\text{Lattice HVP}}$ scenario is imposed, as shown by the gray region. Notably, around $m_S \simeq 62 \text{ GeV}$, the coupling λ_S exhibits a bottleneck shape, a feature driven by the Higgs resonance mechanism. As the DM mass moves away from the resonance, increasingly larger values of λ_S are needed to open up other annihilation channels.

In the same panel, we observe a marginal narrowing of the allowed region when the $m_{W,\text{CDF II}} + \Delta a_\mu^{\text{Lattice HVP}}$ scenario is applied, as indicated by the blue regions. Interestingly, when the $m_{W,\text{CDF II}} + a_\mu^{e^+e^- \text{ HVP}}$ scenario is considered, the constraints on λ_S are slightly

relaxed compared to the other scenarios (red regions). This relaxation occurs because the contribution from $\Delta a_\mu^{e^+e^- \text{ HVP}}$ opens DM annihilation channels dominated by neutrino final states, mediated via the exchange of $n_{1,2}$.

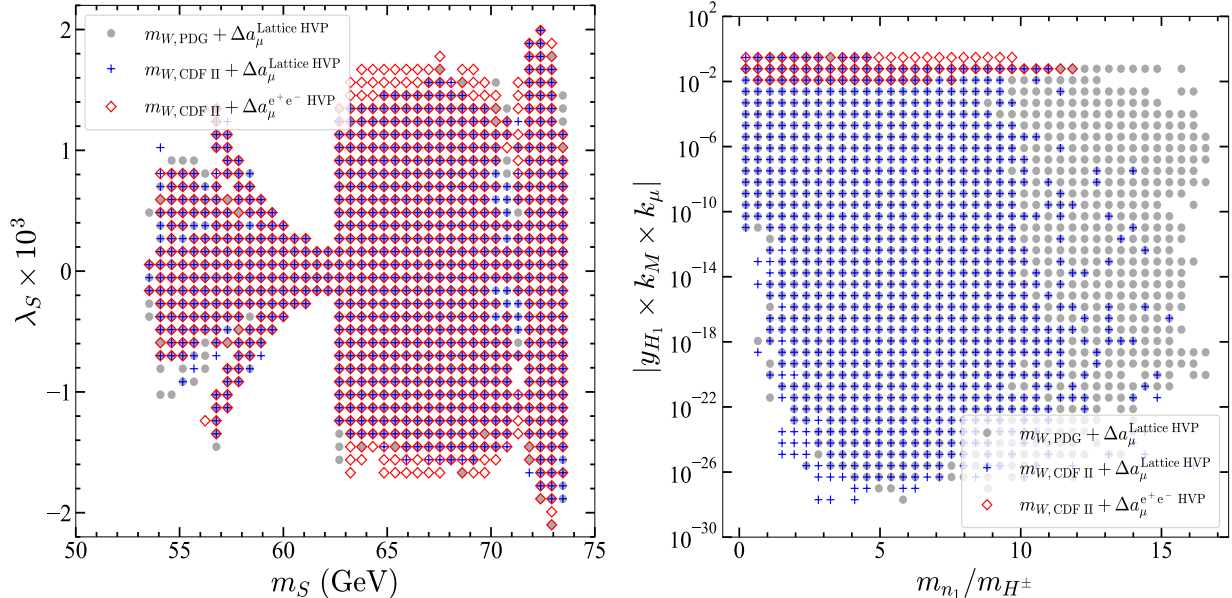


FIG. 6: Left panel: The 95% C.L. regions for the Higgs-DM-DM coupling $\lambda_S \times 10^3$ as a function of the DM mass m_S ; Right panel: The correlation between the product of coupling coefficients $|y_{H_1} \times k_M \times k_\mu|$ and mass spectra m_{n_1}/m_{H^\pm} . The blue cross region favor the CDF II W boson mass, while the definitions of other colors are the same as in Fig. 5.

On the other hand, we show the allowed regions on the mass ratio m_{n_1}/m_{H^\pm} versus coupling coefficients $|y_{H_1} \times k_M \times k_\mu|$ in the right panel of Fig. 6. We find that the mass ratio $m_{n_1}/m_{H^\pm} \gtrsim 1$ in nearly all of the allowed regions. As indicated by Eq. (9), this results in a positive contribution to Δa_μ , aligning with the findings presented in the left panel of Fig. 2. The upper limit on $m_{n_1}/m_{H^\pm} \lesssim 17$ is due to the range of the model parameters under consideration (gray region). The CDF II W mass requires a heavier H^\pm , resulting in a reduced ratio of m_{n_1}/m_{H^\pm} as shown in the blue region. Additionally, considering $\Delta a_\mu^{e^+e^- \text{ HVP}}$, which deviates from the SM prediction by 5.1σ , the coupling coefficients must be sizable to enhance contributions to the muon magnetic moment. Consequently, $|y_{H_1} \times k_M \times k_\mu| \gtrsim 10^{-2}$, as indicated by the red regions in the right panel of Fig. 6.

In the left panel of Fig. 7, we present the allowed regions on the plane of the DM-proton scattering cross-section and the DM mass. We note that the recent results from

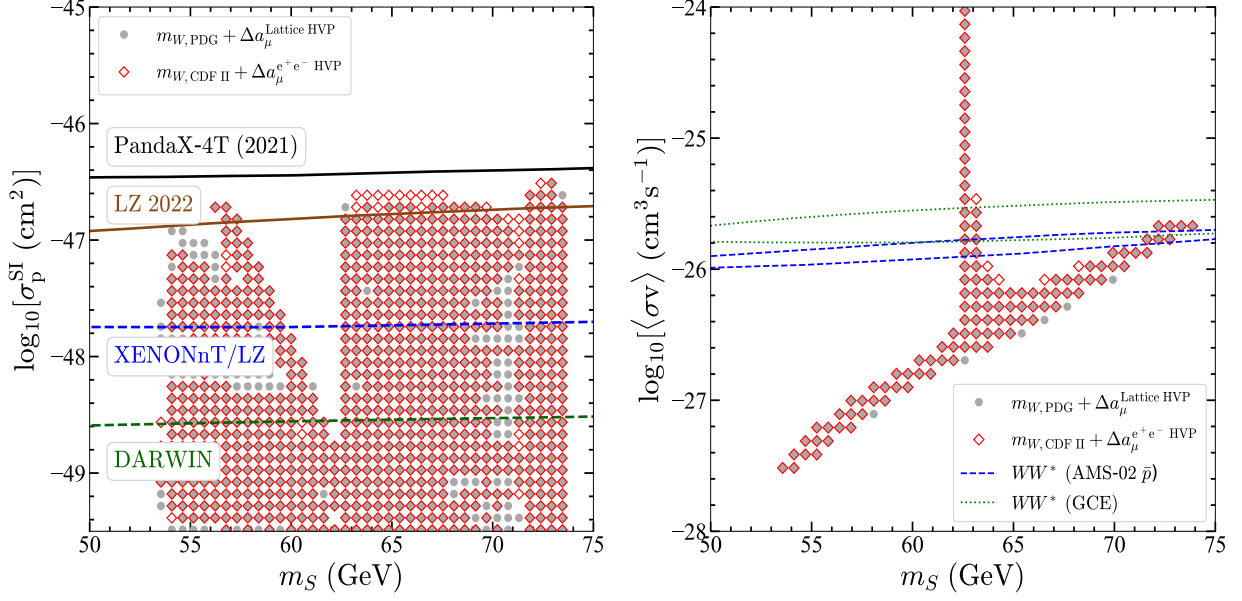


FIG. 7: Left panel: The 95% C.L. regions from all new constraints projected on the $(m_S, \sigma_p^{\text{SI}})$ panel. The solid black and brown lines represent the current constraints set by PandaX-4T (2021) [73] and LZ 2022 [74], respectively. The dashed blue and green lines are the expected detection sensitivity of XENONnT/LZ [75, 76] and DARWIN [77]. Right panel: The 95% C.L. regions on the $(m_S, \langle\sigma v\rangle)$ panel. The dotted green and dashed blue contours indicate the parameter regions that can explain the GCE and AMS-02 \bar{p} excesses through the DM annihilation channel $SS \rightarrow WW^*$ [78].

LZ experiment [74] (brown solid line) has imposed tighter constraints on the DM-proton scattering cross-section compared to the results in Ref. [26]. In this model, the only process that significantly contributes to the DM direct detection rate at tree level is elastic scattering via t-channel Higgs boson exchange. Therefore, λ_S is expected to face tighter constraints, with the allowed regions around the Higgs resonance shrinking further. Outside of this Higgs resonance region, a substantial portion of the viable parameter space in the model can be probed by future DM direct detection experiments, including XENONnT/LZ (dashed blue line) and DARWIN (dashed green line).

However, in cases involving new Z_2 -odd mediators, the real scalar DM-proton scattering cross-sections are suppressed at the loop level. This occurs in processes where H^\pm or A contribute to one-loop box type diagrams involving W/Z bosons, as well as in one-loop Higgs vertex correction diagrams. As a result, there are parameter spaces that remain

below the expected sensitivity of conventional DM direct detection experiments.

We also examine the properties of DM annihilation in indirect detection. In the right panel of Fig. 7, we display the 95% C.L. regions for the DM annihilation cross-section $\langle\sigma v\rangle$ in the present Universe as a function of DM mass m_S . In the case of DM mass $m_S \approx 62.5$ GeV, the annihilation process dominated by the Higgs resonance mechanism exhibits the cross-section at the present time significantly greater than the thermal value of $\langle\sigma v\rangle \sim 10^{-26} \text{ cm}^3\text{s}^{-1}$. On the other hand, we have also confirmed that Higgs resonance and $SS \rightarrow WW^*$ annihilation mechanisms can satisfy the correct DM relic density while providing a natural explanation for the GCE and AMS-02 \bar{p} excess. This corresponds to DM masses around $m_S \approx 62.5$ GeV and $m_S \approx 72$ GeV, respectively.

Finally, we consider several LHC search strategies within this model, including mono-jet, compressed mass spectrum, and other SUSY-like searches, and recast these analyses to impose constraints on the model parameters. For mono-jet searches, the signal signature consists of an energetic jet and significant missing transverse momentum. Depending on whether n_1 is decoupled or not, we specifically classify the following two scenarios:

1. Decoupled n_1 : This scenario is similar to the case in the inert 2HDM, and the signal process is denoted as $pp \rightarrow SS + \text{jets}$. We apply the most restrictive cut-window "IM12" in Table.6 of Ref. [53] from the ATLAS collaboration, which under yields 207 signal events and 223 ± 19 background events and recast this inclusive signal region via `MadAnalysis5` [58]. We can obtain relevant constraints on the coupling λ_S for various DM masses m_S . For $45 \text{ GeV} \lesssim m_S \lesssim \frac{m_h}{2}$, the λ_S values are excluded in the range from 2.15×10^{-2} to 4.20×10^{-2} . As m_S increases, the constraints on λ_S become less stringent. For $\frac{m_h}{2} \lesssim m_S \lesssim 80 \text{ GeV}$, the mediator, Higgs boson, can only be produced off-shell, leading to even weaker constraints on λ_S , ranging from 0.258 to 3.568.
2. Non-decoupled n_1 : In this scenario, in addition to the process above, the process $pp \rightarrow n_1 \bar{n}_1 + \text{jets}$ with $n_1 \rightarrow \nu_l S$ and $\bar{n}_1 \rightarrow \bar{\nu}_l S$ is also involved. We found that the cross section for this process is relatively small, approximately 10^{-2} fb, even assuming a branching ratio of $n_1 \rightarrow \nu_l S$ and $\bar{n}_1 \rightarrow \bar{\nu}_l S$ of 100%. As a result, y_{H1} in the perturbative region cannot be effectively constrained. Nevertheless, since these two processes cannot be distinguished these in the ATLAS detectors, their contributions are combined in this scenario. To obtain a stronger constraint on λ_S , we set $\Delta M_{\Psi\chi} = 1$

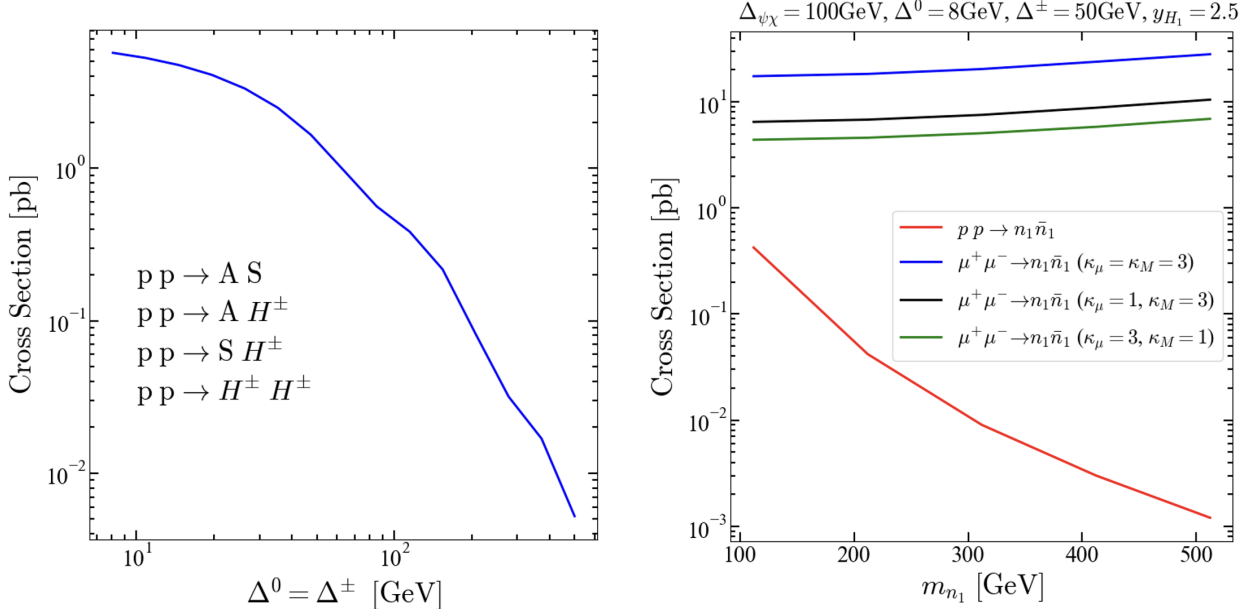


FIG. 8: Left panel: The total production cross section, including $pp \rightarrow AS$, $pp \rightarrow AH^\pm$, $pp \rightarrow SH^\pm$, and $pp \rightarrow H^\pm H^\mp$, is calculated with DM mass $m_S = 60$ GeV while varying the mass splitting $\Delta^{0,\pm}$ at $\sqrt{s} = 13$ TeV. Right panel: The production cross section of $pp \rightarrow n_1\bar{n}_1$ at $\sqrt{s} = 13$ TeV and $\mu^+\mu^- \rightarrow n_1\bar{n}_1$ at $\sqrt{s} = 3$ TeV with varying the mass of n_1 .

GeV with $m_{n_1} = 100$ GeV (minimum mass) and $y_{H_1} = \sqrt{4\pi}$ (maximum coupling). For $45 \text{ GeV} \lesssim m_S \lesssim \frac{m_h}{2}$ and $\frac{m_h}{2} \lesssim m_S \lesssim 80$ GeV, the λ_S values are excluded in the ranges of 2.16×10^{-2} to 3.70×10^{-2} and 0.11 to 3.24, respectively.

Compared to the left panel of Fig. 6, we find that the current mono-jet searches from Ref. [53] still cannot exclude the allowed parameter space for either of these two scenarios.

We then turn to compressed mass spectrum searches. For small mass splitting $\Delta^{0,\pm}$, the signal signatures typically contain soft objects. For example, searches for SUSY particles in final states with two or three soft leptons and missing transverse momentum have been extensively conducted by the CMS [54] and ATLAS [47] collaborations. As in the mono-jet analysis, we classify the signals into two scenarios depending on whether n_1 is decoupled or not:

1. Decoupled n_1 : In this scenario, the heavier neutral scalar A produced at the LHC can decay into a pair of leptons, with the invariant mass of these leptons being sensitive to the mass splitting Δ^0 . We recast the current exclusion limit from the CMS SUSY compressed mass spectrum searches [54] via MadAnalysis5. Specifically, we focus on

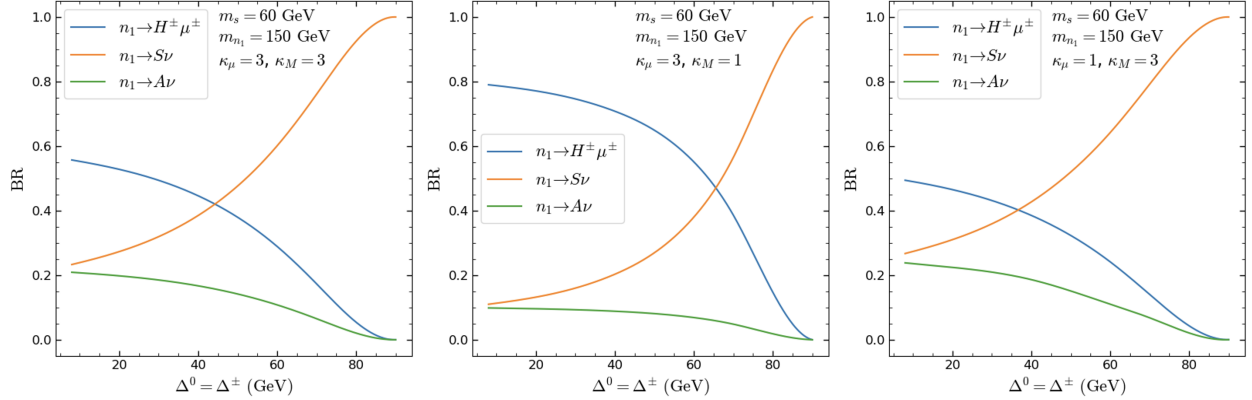


FIG. 9: The decay branching ratios of n_1 with $\Delta^0 = \Delta^\pm$, $m_s = 60$ GeV, and $m_{n_1} = 150$ GeV. Left panel: The scenario where $\kappa_M = \kappa_\mu = 3$; Central panel: The case with $\kappa_\mu = 3$ and $\kappa_M = 1$; Right panel: The configuration with $\kappa_\mu = 1$ and $\kappa_M = 3$.

the exclusive signal region, $2l$ -Ewk SR with $p_T^{\text{miss}} = 200 - 240$ [GeV] and $M(l\bar{l}) = 1 - 4$ [GeV] as outlined in Table 4 of Ref. [54]. In this region, 2 events were observed, while 5.5 ± 2.5 total background events were expected. This exclusive signal region provides the most stringent constraints. We consider all possible signal processes that produce soft leptons signatures, including SA , AH^\pm , and $H^\pm H^\mp$. As shown in the left panel of Fig. 8, the combined cross sections for these processes, without the decays of A and H^\pm , are on the order of a few pb. Moreover, the decay branching ratios of H^\pm are approximately $BR(H^\pm \rightarrow Sjj') \sim 0.67$ and $BR(H^\pm \rightarrow Sl^\pm\nu) \sim 0.33$. Similarly, the branching ratios for A are $BR(A \rightarrow Sjj) \sim 0.66$, $BR(A \rightarrow Sl^+l^-) \sim 0.12$, and $BR(A \rightarrow S\nu\bar{\nu}) \sim 0.22$. In the parameter space of interest, these branching ratios show slight dependence on the mass splitting $\Delta^{0,\pm}$. However, these cross sections are still not large enough to exclude the parameter space for the dominant SA co-annihilation region, except for $m_S \lesssim 60$ GeV with $\Delta^0 < 10$ GeV, as indicated by the black solid line in the upper-right panel of Fig. 5. Note that $\Delta^\pm = 50$ GeV is fixed in this analysis. The magnitude of the mass splitting inversely correlates with the stringency of the imposed constraints. Specifically, larger mass splittings result in less stringent restrictions, while smaller mass splittings enforce stricter constraints. However, the overall impact on the exclusion line remains relatively modest. As we will see in Sec. IV C, the upcoming luminosity upgrade of the LHC will thoroughly test the entire SA co-annihilation region.

2. Non-decoupled n_1 : In this scenario, we first consider the new process of generating soft leptons from $n_1\bar{n}_1$ production. Both n_1 and \bar{n}_1 subsequently decay either directly to S or undergo a cascade decay via A and/or H^\pm , yielding soft leptons plus missing transverse momentum. We demonstrate the production cross section for the process $pp \rightarrow n_1\bar{n}_1$ in the right panel of Fig. 8 and find that it decreases notably with increasing m_{n_1} . Here $y_{H_1} = 2.5$, $\Delta_{\Psi\chi} = 100$ GeV, $\kappa_\mu = \kappa_M = 0.1$ are fixed. Moreover, the decay modes of n_1 depend on the mass splitting $\Delta^{0,\pm}$, and we find that the decay channel $n_1 \rightarrow S\nu_l$ becomes dominant for the compressed mass spectrum, as shown in Fig. 9. Here, we fixed $m_s = 60$ GeV and $m_{n_1} = 150$ GeV for the demonstration purpose. Therefore, we conclude that the cross sections for this process are considerably small and lies far beyond the current detection capabilities at the LHC. In the end, although we combine these two types of processes in this scenario for the recasting, the exclusion regions are almost the same as those shown in the upper-right panel of Fig. 5.

Additionally, we investigate the SA , AH^\pm , and $H^\pm H^\mp$ production processes with larger mass splitting $\Delta^{0,\pm}$ to generate 2-leptons ($2l$) or 3-leptons ($3l$) final states. Using MadAnalysis5, we recast the analyses from the ATLAS and CMS collaborations [32, 33, 79], specifically focusing on the ranges $100 \text{ GeV} \lesssim \Delta^{0,\pm} < 500 \text{ GeV}$. Unfortunately, our findings indicate that the larger mass splitting regions of $\Delta^{0,\pm}$ remain largely unexplored due to the very small cross sections shown in the left panel of Fig. 8. As a result, a significant portion of the parameter space remains untested with the current LHC data.

C. Future predictions at collider experiments

We further employ the rescaling method to estimate future bounds in this model at the LHC with increased luminosity. The detailed calculation procedure is as follows: We first estimate the future signal events (s) and background events (b) as

$$s = \sigma_f \epsilon \mathcal{L}_f, \quad (21)$$

$$b = b_c \times \frac{\mathcal{L}_f}{\mathcal{L}_c}, \quad (22)$$

where σ_f represents the future signal cross section, and ϵ denotes the signal efficiency, which we assume remains the same as in the current analysis obtained from the recasting using

MadAnalysis5. The future luminosity is denoted by \mathcal{L}_f . Here, b_c and \mathcal{L}_c represent the current background events and luminosity, respectively. Next, the statistical significance of the observed signal is calculated using the following formula:

$$Z = \sqrt{2 \cdot \left[(s+b) \cdot \ln \left(\frac{(s+b)(b+\sigma_b^2)}{b^2 + (s+b)\sigma_b^2} \right) - \frac{b^2}{\sigma_b^2} \cdot \ln \left(1 + \frac{\sigma_b^2 s}{b(b+\sigma_b^2)} \right) \right]}, \quad (23)$$

where σ_b represents the estimated systematic uncertainty of the background events. A statistical significance corresponding to a 95% confidence level ($Z = 1.96$), is used to estimate the future bounds.

In the decoupled n_1 scenario, the signal cross sections are proportional to the square of the λ_S values. Consequently, we can translate future bounds on σ_f to constraints on λ_S . As examples, for three different assumptions regarding the systematic uncertainty of the background events at the High-Luminosity LHC ($\mathcal{L} = 3000 \text{ fb}^{-1}$), the estimated future bounds for $m_S = 55 \text{ GeV}$ are follows: $\lambda_S \lesssim 6 \times 10^{-3}$ for $\sigma_b/b \sim 0$, $\lambda_S \lesssim 0.018$ for $\sigma_b/b = 10\%$, and $\lambda_S \lesssim 0.026$ for $\sigma_b/b = 20\%$. These results indicate that level of systematic uncertainties becomes a critical factor in predicting future bounds on λ_S . Using the same method as described above, we also analyze the mono-jet signature in the non-decoupled n_1 scenario at the LHC with $\mathcal{L} = 3000 \text{ fb}^{-1}$. However, even with increased luminosity, the constraint on $|y_{H_1}|$ remains difficult to achieve below $\sqrt{4\pi}$. For instance, with $m_S = 55 \text{ GeV}$, $m_{n_1} = 100 \text{ GeV}$, and $\Delta_{\psi\chi} = 1 \text{ GeV}$, the required luminosity to constrain $|y_{H_1}| < \sqrt{4\pi}$ is approximately 3440 fb^{-1} without involving systematic uncertainties.

For the analysis of compressed mass spectra, we also estimate the future bounds at a 95% confidence level for two scenarios under increased luminosity:

1. Decoupled n_1 : In this scenario, significant constraints have already been imposed with the current LHC luminosity. We set the future luminosity to $\mathcal{L}=300fb^{-1}$ for the Run-3 LHC. Given the small number of observed events and the relatively large uncertainties in background events within the exclusive signal region, $2l$ -Ewk SR with $p_T^{\text{miss}} = 200 - 240 \text{ [GeV]}$ and $M(l\ell) = 1 - 4 \text{ [GeV]}$ as outlined in Table 4 of Ref. [54], we conservatively assume a maximum systematic uncertainty of $\sigma_b/b = 45\%$ for the SM background estimation. Under these conditions, we find that the entire parameter space can be excluded, as shown by the green dashed line in the upper-right panel of Fig. 5.

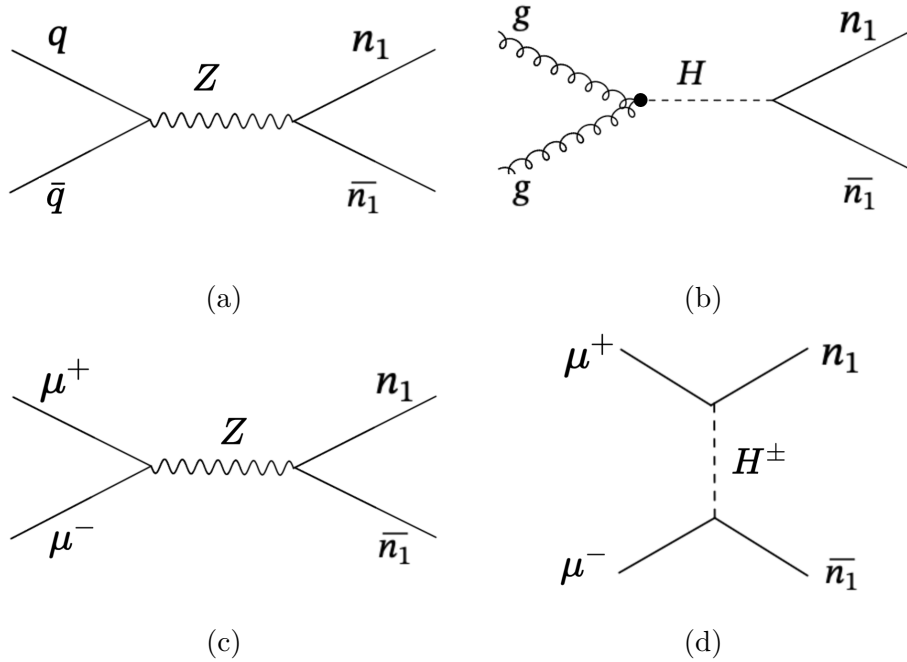


FIG. 10: Feynman diagrams illustrating the $pp \rightarrow n_1 \bar{n}_1$ are shown in subfigures (a) and (b), while subfigures (c) and (d) represent the Feynman diagram for the $\mu^+ \mu^- \rightarrow n_1 \bar{n}_1$.

2. Non-decoupled n_1 : In contrast, we find that even with a future luminosity of 3000 fb^{-1} , the parameter $|y_{H_1}|$ cannot be effectively constrained to below $\sqrt{4\pi}$ in this scenario. For instance, taking $m_S = 55 \text{ GeV}$, $\Delta_{\psi\chi} = 1 \text{ GeV}$, $\Delta^0 = \Delta^\pm = 8 \text{ GeV}$, and $m_{n_1} = 100 \text{ GeV}$ as an example, the required luminosity to constrain $|y_{H_1}| < \sqrt{4\pi}$ is approximately $\mathcal{L} = 3850 \text{ fb}^{-1}$, without taking into account systematic uncertainties.

The small cross sections of the non-decoupled n_1 in compressed mass spectra make them difficult to detect effectively at the LHC, partly due to the decay branching ratios of n_1 . To address this, we studied the relationship between the n_1 decay branching ratios and the mass splittings, $\Delta^0 = \Delta^\pm$, under different coupling values of κ_M and κ_μ , as shown in Fig. 9. Our findings demonstrate that simultaneous variations in κ_M and κ_μ do not affect the overall decay branching ratio (left panel). Specifically, while κ_M governs interactions with μ_L^\pm and ν^\pm , and κ_μ is exclusively related to μ_R^\pm , setting $\kappa_M = 1$ and $\kappa_\mu = 3$ (central panel) leads to a significant increase in the branching ratio of the $n_1 \rightarrow H^\pm \mu^\mp$ decay channel. Conversely, when $\kappa_M = 3$ and $\kappa_\mu = 1$ (right panel), there is a marked increase in the branching ratios of the $n_1 \rightarrow A\nu$ and $n_1 \rightarrow S\nu$ decay channels. Thus, studying the decay branching ratios of n_1 offers insight into the relative magnitudes of the couplings κ_M and κ_μ .

Finally, since the future bounds for this model at the High-Luminosity LHC remain limited, our study further explores the potential of high-energy muon colliders. With a center-of-mass energy of 3 TeV [80, 81], these next-generation facilities could significantly improve the prospects of detecting the $n_1\bar{n}_1$ production process. The key difference lies in the interaction type: the $\mu^+\mu^- \rightarrow n_1\bar{n}_1$ process primarily occurs via t -channel H^\pm exchange, while the $pp \rightarrow n_1\bar{n}_1$ process is dominated by the Drell-Yan process. The relevant Feynman diagrams for these processes are shown in Fig. 10. As illustrated in the right panel of Fig. 8, the cross sections for $\mu^+\mu^- \rightarrow n_1\bar{n}_1$ with couplings $\kappa_\mu = \kappa_M = 3$ (orange line) significantly surpass those of the $pp \rightarrow n_1\bar{n}_1$ process (blue line), and crucially, do not decrease as m_{n_1} increases. In this figure, we fixed $\Delta_{\psi\chi} = 100$ GeV, $\Delta^0 = 8$ GeV, $\Delta^\pm = 50$ GeV, and $y_{H_1} = 2.5$ for the demonstration purpose. Additionally, we varied the ratios of couplings κ_μ and κ_M , with $\kappa_\mu = 1$ and $\kappa_M = 3$ (green line), and $\kappa_\mu = 3$ and $\kappa_M = 1$ (red line), for the $\mu^+\mu^- \rightarrow n_1\bar{n}_1$ process, as shown in the right panel of Fig. 8. It is clear that the production cross sections in this process are sensitive to the relative magnitudes of κ_μ and κ_M , similar to their influence on n_1 decay branching ratios. Thus, a future muon collider could be an ideal platform for detecting signals of this process.

V. CONCLUSION

In this work, we present a DM model that extends the particle SM by incorporating singlet and doublet Z_2 -odd Dirac fermion fields, alongside a Z_2 -odd doublet complex scalar field. This simple DM model holds the capacity to elucidate the excesses observed in the precision measurements of the muon magnetic moment and the W boson mass from Fermilab experiments, along with addressing the Galactic Center GeV excess (GCE) and the AMS-02 antiproton (\bar{p}) excess.

We summarize the characteristics of the feasible parameter regions as follows: First, the mass of the scalar DM within the range of 53 to 74 GeV remains allowed, regardless of the anomalies in the muon magnetic moment and the W boson mass, as shown in Fig. 5. Second, both the inert Higgs sector and the new Dirac fermions contribute to the W boson mass as illustrated in Fig. 3. Therefore, a smaller charged mass splitting, Δ^\pm , is still permissible for explaining the W boson mass excess, which is notable difference from the inert two-Higgs-doublet models [26]. Third, the co-annihilation dominant regions with neutral mass

splitting $\Delta^0 \lesssim 10$ GeV are strongly constrained by current and forthcoming LHC searches, as indicated in Fig. 5. Fourth, although the recent LZ results exclude a substantial portion of the parameter space around the Higgs resonance, smaller λ_S values are still allowed and remain challenging to probe in future DM direct detection experiments. Fifth, there are small regions for DM masses around 63 GeV and 71 – 73 GeV that can simultaneously explain both the GCE and the AMS-02 \bar{p} excess, as seen in the right panel of Fig. 7. Finally, the model parameters y_{H_1} , k_M , and k_μ , along with the neutral dark fermion mass, are crucial for explaining the muon magnetic moment excess, as shown in the right panel of Fig. 6. However, these parameters are difficult to examine at the LHC. Fortunately, a high-energy muon collider may provide an ideal environment to detect them, potentially confirming or ruling out the predictions in this model.

Before closing, we would like to offer the following remarks for this DM model: (1) While our focus has been on selecting the scalar field S as the DM candidate in this study, it is worth noting that the fermion field n_1 could also serve as a DM candidate when $m_{n_1} < m_S$. This intriguing possibility remains open for exploration in future investigations [42]. (2) The multi-muons plus missing energy serves as a common signature arising from processes involving ψ^\pm and n_2 [82–84]. These distinctive signals warrant investigation at high luminosity large hadron colliders and potential future muon colliders. (3) Similar to the inert two Higgs doublet model [85] and the model incorporating vector-like leptons and scalar singlets [86], which are capable of inducing strong first-order phase transitions (SFOPT), our model also holds the potential to trigger SFOPT. This possibility invites further study and exploration in the future.

ACKNOWLEDGMENTS

This work was supported by the National Key Research and Development Program of China (No. 2022YFF0503304), and the Project for Young Scientists in Basic Research of the Chinese Academy of Sciences (No. YSBR-092). CTL and XYL are supported by the National Natural Science Foundation of China (NNSFC) under grant No. 12335005 and the Special funds for postdoctoral overseas recruitment, Ministry of Education of China (No. 164080H0262403). This work was also supported in part by the NNSFC under grant Nos. 19Z103010239 and 12350410369, and Vietnam National Foundation for Science and

Technology Development (NAFOSTED) under grant number 103.01-2023.50 (VQT). VQT would like to thank the Medium and High Energy Physics group at the Institute of Physics, Academia Sinica for their hospitality during the course of this work.

- [1] D. P. Aguillard *et al.* [Muon g-2], *Phys. Rev. Lett.* **131**, no.16, 161802 (2023) doi:10.1103/PhysRevLett.131.161802 [arXiv:2308.06230 [hep-ex]].
- [2] T. Aoyama, N. Asmussen, M. Benayoun, J. Bijnens, T. Blum, M. Bruno, I. Caprini, C. M. Carloni Calame, M. Cè and G. Colangelo, *et al.* *Phys. Rept.* **887**, 1-166 (2020) doi:10.1016/j.physrep.2020.07.006 [arXiv:2006.04822 [hep-ph]].
- [3] S. Borsanyi, Z. Fodor, J. N. Guenther, C. Hoelbling, S. D. Katz, L. Lellouch, T. Lippert, K. Miura, L. Parato and K. K. Szabo, *et al.* *Nature* **593**, no.7857, 51-55 (2021) doi:10.1038/s41586-021-03418-1 [arXiv:2002.12347 [hep-lat]].
- [4] T. Aaltonen *et al.* [CDF], *Science* **376**, no.6589, 170-176 (2022) doi:10.1126/science.abk1781
- [5] [ATLAS], ATLAS-CONF-2023-004.
- [6] [CMS], CMS-PAS-SMP-23-00.
- [7] M. Roos, [arXiv:1001.0316 [astro-ph.CO]].
- [8] G. Arcadi, M. Dutra, P. Ghosh, M. Lindner, Y. Mambrini, M. Pierre, S. Profumo and F. S. Queiroz, *Eur. Phys. J. C* **78**, no.3, 203 (2018) doi:10.1140/epjc/s10052-018-5662-y [arXiv:1703.07364 [hep-ph]].
- [9] M. Bauer and T. Plehn, *Lect. Notes Phys.* **959**, pp. (2019) Springer, 2019, doi:10.1007/978-3-030-16234-4 [arXiv:1705.01987 [hep-ph]].
- [10] M. Schumann, *J. Phys. G* **46**, no.10, 103003 (2019) doi:10.1088/1361-6471/ab2ea5 [arXiv:1903.03026 [astro-ph.CO]].
- [11] T. R. Slatyer, *SciPost Phys. Lect. Notes* **53**, 1 (2022) doi:10.21468/SciPostPhysLectNotes.53 [arXiv:2109.02696 [hep-ph]].
- [12] A. Boveia and C. Doglioni, *Ann. Rev. Nucl. Part. Sci.* **68**, 429-459 (2018) doi:10.1146/annurev-nucl-101917-021008 [arXiv:1810.12238 [hep-ex]].
- [13] J. Aalbers *et al.* [LZ], *Phys. Rev. Lett.* **131**, no.4, 041002 (2023) doi:10.1103/PhysRevLett.131.041002 [arXiv:2207.03764 [hep-ex]].

- [14] E. Aprile *et al.* [XENON], Phys. Rev. Lett. **131**, no.4, 041003 (2023) doi:10.1103/PhysRevLett.131.041003 [arXiv:2303.14729 [hep-ex]].
- [15] D. Perez Adan [ATLAS and CMS], [arXiv:2301.10141 [hep-ex]].
- [16] D. Hooper and L. Goodenough, Phys. Lett. B **697**, 412-428 (2011) doi:10.1016/j.physletb.2011.02.029 [arXiv:1010.2752 [hep-ph]].
- [17] B. Zhou, Y. F. Liang, X. Huang, X. Li, Y. Z. Fan, L. Feng and J. Chang, Phys. Rev. D **91**, no.12, 123010 (2015) doi:10.1103/PhysRevD.91.123010 [arXiv:1406.6948 [astro-ph.HE]].
- [18] F. Calore, I. Cholis and C. Weniger, JCAP **03**, 038 (2015) doi:10.1088/1475-7516/2015/03/038 [arXiv:1409.0042 [astro-ph.CO]].
- [19] T. Daylan, D. P. Finkbeiner, D. Hooper, T. Linden, S. K. N. Portillo, N. L. Rodd and T. R. Slatyer, Phys. Dark Univ. **12**, 1-23 (2016) doi:10.1016/j.dark.2015.12.005 [arXiv:1402.6703 [astro-ph.HE]].
- [20] M. Y. Cui, Q. Yuan, Y. L. S. Tsai and Y. Z. Fan, Phys. Rev. Lett. **118**, no.19, 191101 (2017) doi:10.1103/PhysRevLett.118.191101 [arXiv:1610.03840 [astro-ph.HE]].
- [21] A. Cuoco, M. Krämer and M. Korsmeier, Phys. Rev. Lett. **118**, no.19, 191102 (2017) doi:10.1103/PhysRevLett.118.191102 [arXiv:1610.03071 [astro-ph.HE]].
- [22] M. Y. Cui, X. Pan, Q. Yuan, Y. Z. Fan and H. S. Zong, JCAP **06**, 024 (2018) doi:10.1088/1475-7516/2018/06/024 [arXiv:1803.02163 [astro-ph.HE]].
- [23] I. Cholis, T. Linden and D. Hooper, Phys. Rev. D **99**, no.10, 103026 (2019) doi:10.1103/PhysRevD.99.103026 [arXiv:1903.02549 [astro-ph.HE]].
- [24] H. Okada, T. Toma and K. Yagyu, Phys. Rev. D **90**, 095005 (2014) doi:10.1103/PhysRevD.90.095005 [arXiv:1408.0961 [hep-ph]].
- [25] M. E. Peskin and T. Takeuchi, Phys. Rev. D **46**, 381-409 (1992) doi:10.1103/PhysRevD.46.381
- [26] Y. Z. Fan, T. P. Tang, Y. L. S. Tsai and L. Wu, Phys. Rev. Lett. **129**, no.9, 091802 (2022) doi:10.1103/PhysRevLett.129.091802 [arXiv:2204.03693 [hep-ph]].
- [27] E. Ma, Phys. Rev. D **73**, 077301 (2006) doi:10.1103/PhysRevD.73.077301 [arXiv:hep-ph/0601225 [hep-ph]].
- [28] D. Sokolowska, [arXiv:1107.1991 [hep-ph]].
- [29] T. Abe and R. Sato, JHEP **03**, 109 (2015) doi:10.1007/JHEP03(2015)109 [arXiv:1501.04161 [hep-ph]].

- [30] S. Banerjee, F. Boudjema, N. Chakrabarty, G. Chalons and H. Sun, *Phys. Rev. D* **100**, no.9, 095024 (2019) doi:10.1103/PhysRevD.100.095024 [arXiv:1906.11269 [hep-ph]].
- [31] Y. L. S. Tsai, V. Q. Tran and C. T. Lu, *JHEP* **06**, 033 (2020) doi:10.1007/JHEP06(2020)033 [arXiv:1912.08875 [hep-ph]].
- [32] G. Aad *et al.* [ATLAS], *Eur. Phys. J. C* **80**, no.2, 123 (2020) doi:10.1140/epjc/s10052-019-7594-6 [arXiv:1908.08215 [hep-ex]].
- [33] A. M. Sirunyan *et al.* [CMS], *JHEP* **04**, 123 (2021) doi:10.1007/JHEP04(2021)123 [arXiv:2012.08600 [hep-ex]].
- [34] L. Calibbi, R. Ziegler and J. Zupan, *JHEP* **07**, 046 (2018) doi:10.1007/JHEP07(2018)046 [arXiv:1804.00009 [hep-ph]].
- [35] G. Arcadi, L. Calibbi, M. Fedele and F. Mescia, *Phys. Rev. Lett.* **127**, no.6, 061802 (2021) doi:10.1103/PhysRevLett.127.061802 [arXiv:2104.03228 [hep-ph]].
- [36] P. Arnan, A. Crivellin, M. Fedele and F. Mescia, *JHEP* **06**, 118 (2019) doi:10.1007/JHEP06(2019)118 [arXiv:1904.05890 [hep-ph]].
- [37] R. Barbieri, L. J. Hall and V. S. Rychkov, *Phys. Rev. D* **74**, 015007 (2006) doi:10.1103/PhysRevD.74.015007 [arXiv:hep-ph/0603188 [hep-ph]].
- [38] A. Arhrib, R. Benbrik and N. Gaur, *Phys. Rev. D* **85**, 095021 (2012) doi:10.1103/PhysRevD.85.095021 [arXiv:1201.2644 [hep-ph]].
- [39] B. Świeżewska, *Phys. Rev. D* **88**, no.5, 055027 (2013) [erratum: *Phys. Rev. D* **88**, no.11, 119903 (2013)] doi:10.1103/PhysRevD.88.055027 [arXiv:1209.5725 [hep-ph]].
- [40] D. Eriksson, J. Rathsman and O. Stal, *Comput. Phys. Commun.* **181**, 189-205 (2010) doi:10.1016/j.cpc.2009.09.011 [arXiv:0902.0851 [hep-ph]].
- [41] F. D'Eramo, *Phys. Rev. D* **76**, 083522 (2007) doi:10.1103/PhysRevD.76.083522 [arXiv:0705.4493 [hep-ph]].
- [42] S. Bhattacharya, P. Ghosh, N. Sahoo and N. Sahu, *Front. in Phys.* **7**, 80 (2019) doi:10.3389/fphy.2019.00080 [arXiv:1812.06505 [hep-ph]].
- [43] K. A. Olive *et al.* [Particle Data Group], *Chin. Phys. C* **38**, 090001 (2014) doi:10.1088/1674-1137/38/9/090001
- [44] E. Lundstrom, M. Gustafsson and J. Edsjo, *Phys. Rev. D* **79**, 035013 (2009) doi:10.1103/PhysRevD.79.035013 [arXiv:0810.3924 [hep-ph]].

- [45] N. Blinov, J. Kozaczuk, D. E. Morrissey and A. de la Puente, *Phys. Rev. D* **93**, no.3, 035020 (2016) doi:10.1103/PhysRevD.93.035020 [arXiv:1510.08069 [hep-ph]].
- [46] G. Abbiendi *et al.* [OPAL], *Eur. Phys. J. C* **32**, 453-473 (2004) doi:10.1140/epjc/s2003-01466-y [arXiv:hep-ex/0309014 [hep-ex]].
- [47] G. Aad *et al.* [ATLAS], *Phys. Rev. D* **101**, no.5, 052005 (2020) doi:10.1103/PhysRevD.101.052005 [arXiv:1911.12606 [hep-ex]].
- [48] G. Aad *et al.* [ATLAS], *Phys. Lett. B* **842**, 137963 (2023) doi:10.1016/j.physletb.2023.137963 [arXiv:2301.10731 [hep-ex]].
- [49] [ATLAS], ATLAS-CONF-2020-027.
- [50] G. Aad *et al.* [ATLAS], *JHEP* **07**, 088 (2023) doi:10.1007/JHEP07(2023)088 [arXiv:2207.00348 [hep-ex]].
- [51] A. M. Sirunyan *et al.* [CMS], *JHEP* **07**, 027 (2021) doi:10.1007/JHEP07(2021)027 [arXiv:2103.06956 [hep-ex]].
- [52] B. Swiezewska and M. Krawczyk, *Phys. Rev. D* **88**, no.3, 035019 (2013) doi:10.1103/PhysRevD.88.035019 [arXiv:1212.4100 [hep-ph]].
- [53] G. Aad *et al.* [ATLAS], *Phys. Rev. D* **103**, no.11, 112006 (2021) doi:10.1103/PhysRevD.103.112006 [arXiv:2102.10874 [hep-ex]].
- [54] A. Tumasyan *et al.* [CMS], *JHEP* **04**, 091 (2022) doi:10.1007/JHEP04(2022)091 [arXiv:2111.06296 [hep-ex]].
- [55] J. Alwall, R. Frederix, S. Frixione, V. Hirschi, F. Maltoni, O. Mattelaer, H. S. Shao, T. Stelzer, P. Torrielli and M. Zaro, *JHEP* **07**, 079 (2014) doi:10.1007/JHEP07(2014)079 [arXiv:1405.0301 [hep-ph]].
- [56] T. Sjöstrand, S. Ask, J. R. Christiansen, R. Corke, N. Desai, P. Ilten, S. Mrenna, S. Prestel, C. O. Rasmussen and P. Z. Skands, *Comput. Phys. Commun.* **191**, 159-177 (2015) doi:10.1016/j.cpc.2015.01.024 [arXiv:1410.3012 [hep-ph]].
- [57] J. de Favereau *et al.* [DELPHES 3], *JHEP* **02**, 057 (2014) doi:10.1007/JHEP02(2014)057 [arXiv:1307.6346 [hep-ex]].
- [58] B. Dumont, B. Fuks, S. Kraml, S. Bein, G. Chalons, E. Conte, S. Kulkarni, D. Sengupta and C. Wymant, *Eur. Phys. J. C* **75**, no.2, 56 (2015) doi:10.1140/epjc/s10052-014-3242-3 [arXiv:1407.3278 [hep-ph]].

- [59] G. Bélanger, F. Boudjema, A. Goudelis, A. Pukhov and B. Zaldivar, *Comput. Phys. Commun.* **231**, 173-186 (2018) doi:10.1016/j.cpc.2018.04.027 [arXiv:1801.03509 [hep-ph]].
- [60] P. A. R. Ade *et al.* [Planck], *Astron. Astrophys.* **594**, A25 (2016) doi:10.1051/0004-6361/201526803 [arXiv:1506.06660 [astro-ph.GA]].
- [61] K. A. Olive *et al.* [Particle Data Group], *Chin. Phys. C* **38**, 090001 (2014) doi:10.1088/1674-1137/38/9/090001
- [62] G. Abbiendi *et al.* [OPAL], *Eur. Phys. J. C* **32**, 453-473 (2004) doi:10.1140/epjc/s2003-01466-y [arXiv:hep-ex/0309014 [hep-ex]].
- [63] N. Aghanim *et al.* [Planck], *Astron. Astrophys.* **641**, A6 (2020) [erratum: *Astron. Astrophys.* **652**, C4 (2021)] doi:10.1051/0004-6361/201833910 [arXiv:1807.06209 [astro-ph.CO]].
- [64] [ATLAS], ATLAS-CONF-2018-031.
- [65] R. L. Workman *et al.* [Particle Data Group], *PTEP* **2022**, 083C01 (2022) doi:10.1093/ptep/ptac097
- [66] W. A. Rolke, A. M. Lopez and J. Conrad, *Nucl. Instrum. Meth. A* **551**, 493-503 (2005) doi:10.1016/j.nima.2005.05.068 [arXiv:physics/0403059 [physics]].
- [67] A. Albert *et al.* [Fermi-LAT and DES], *Astrophys. J.* **834**, no.2, 110 (2017) doi:10.3847/1538-4357/834/2/110 [arXiv:1611.03184 [astro-ph.HE]].
- [68] M. Y. Cui, Q. Yuan, Y. L. S. Tsai and Y. Z. Fan, *Phys. Rev. Lett.* **118**, no.19, 191101 (2017) doi:10.1103/PhysRevLett.118.191101 [arXiv:1610.03840 [astro-ph.HE]].
- [69] A. Cuoco, M. Krämer and M. Korsmeier, *Phys. Rev. Lett.* **118**, no.19, 191102 (2017) doi:10.1103/PhysRevLett.118.191102 [arXiv:1610.03071 [astro-ph.HE]].
- [70] M. Y. Cui, X. Pan, Q. Yuan, Y. Z. Fan and H. S. Zong, *JCAP* **06**, 024 (2018) doi:10.1088/1475-7516/2018/06/024 [arXiv:1803.02163 [astro-ph.HE]].
- [71] I. Cholis, T. Linden and D. Hooper, *Phys. Rev. D* **99**, no.10, 103026 (2019) doi:10.1103/PhysRevD.99.103026 [arXiv:1903.02549 [astro-ph.HE]].
- [72] D. Foreman-Mackey, D. W. Hogg, D. Lang and J. Goodman, *Publ. Astron. Soc. Pac.* **125**, 306-312 (2013) doi:10.1086/670067 [arXiv:1202.3665 [astro-ph.IM]].
- [73] Y. Meng *et al.* [PandaX-4T], *Phys. Rev. Lett.* **127**, no.26, 261802 (2021) doi:10.1103/PhysRevLett.127.261802 [arXiv:2107.13438 [hep-ex]].
- [74] J. Aalbers *et al.* [LZ], *Phys. Rev. Lett.* **131**, no.4, 041002 (2023) doi:10.1103/PhysRevLett.131.041002 [arXiv:2207.03764 [hep-ex]].

- [75] E. Aprile *et al.* [XENON], JCAP **11**, 031 (2020) doi:10.1088/1475-7516/2020/11/031 [arXiv:2007.08796 [physics.ins-det]].
- [76] D. S. Akerib *et al.* [LZ], [arXiv:1509.02910 [physics.ins-det]].
- [77] M. Schumann, L. Baudis, L. Büttikofer, A. Kish and M. Selvi, JCAP **10**, 016 (2015) doi:10.1088/1475-7516/2015/10/016 [arXiv:1506.08309 [physics.ins-det]].
- [78] C. R. Zhu, M. Y. Cui, Z. Q. Xia, Z. H. Yu, X. Huang, Q. Yuan and Y. Z. Fan, Phys. Rev. Lett. **129**, no.23, 23 (2022) doi:10.1103/PhysRevLett.129.231101 [arXiv:2204.03767 [astro-ph.HE]].
- [79] G. Aad *et al.* [ATLAS], Phys. Rev. D **101**, no.7, 072001 (2020) doi:10.1103/PhysRevD.101.072001 [arXiv:1912.08479 [hep-ex]].
- [80] J. de Blas *et al.* [Muon Collider], [arXiv:2203.07261 [hep-ph]].
- [81] K. M. Black, S. Jindariani, D. Li, F. Maltoni, P. Meade, D. Stratakis, D. Acosta, R. Agarwal, K. Agashe and C. Aimè, *et al.* JINST **19**, no.02, T02015 (2024) doi:10.1088/1748-0221/19/02/T02015 [arXiv:2209.01318 [hep-ex]].
- [82] S. Bißmann, G. Hiller, C. Hormigos-Feliu and D. F. Litim, Eur. Phys. J. C **81**, no.2, 101 (2021) doi:10.1140/epjc/s10052-021-08886-3 [arXiv:2011.12964 [hep-ph]].
- [83] G. Aad *et al.* [ATLAS], JHEP **07**, 167 (2021) doi:10.1007/JHEP07(2021)167 [arXiv:2103.11684 [hep-ex]].
- [84] C. T. Lu, R. Ramos and Y. L. S. Tsai, JHEP **08**, 073 (2021) doi:10.1007/JHEP08(2021)073 [arXiv:2104.04503 [hep-ph]].
- [85] N. Blinov, S. Profumo and T. Stefaniak, JCAP **07**, 028 (2015) doi:10.1088/1475-7516/2015/07/028 [arXiv:1504.05949 [hep-ph]].
- [86] N. F. Bell, M. J. Dolan, L. S. Friedrich, M. J. Ramsey-Musolf and R. R. Volkas, JHEP **09**, 012 (2019) doi:10.1007/JHEP09(2019)012 [arXiv:1903.11255 [hep-ph]].